RSC Advances

PAPER

View Article Online
View Journal | View Issue

Check for updates

Cite this: *RSC Adv.*, 2026, **16**, 29775

Mn_3O_4/biochar catalyst for enhanced PMS activation and antibiotic degradation *via* radical and non-radical pathways

Muhammad Aadil, †*[a] Md Rezaul Karim,†[b] Abdul Rauf,[c] Mohamed Abdel Rafea,[d] Imran Shakir,[e] Tasneem I. Hussein,[f] Nissren Tamam,[g] Aeshah Alrubayyi[h] and Noureddine Elboughdiri[i]

Metronidazole (MNZ) presents a significant threat to both human health and aquatic environments due to its environmental stability, antimicrobial properties, and capacity to promote drug resistance. Despite this, the effective and environmentally sound elimination of this compound remains a significant hurdle. This study introduces a hydrothermal and co-precipitation approach to synthesize a Mn_3O_4/biochar composite catalyst. This catalyst was engineered to activate peroxymonosulfate (PMS) and thereby expedite the removal of MNZ. The Mn_3O_4/biochar/PMS system exhibited outstanding catalytic efficacy, achieving a complete removal and a kinetic constant of 0.1402 min^{-1} within a 30 minute timeframe under optimal conditions. The degradation of MNZ was consistently effective under various conditions, including different catalyst amounts, concentrations of PMS, initial pollutant concentrations, initial pH levels, the presence of inorganic anions, humic acid, and different water sources. The identification of reactive species through quenching experiments corroborated that sulfate ($SO_4^{\bullet-}$) and hydroxyl radicals ($^{\bullet}OH$) were the main contributing factors in activating PMS for MNZ degradation, along with the minor contribution of singlet oxygen ($^1O_2$). Mechanistic studies also revealed that the efficient activation of PMS was facilitated by redox cycling between $Mn^{2+}/Mn^{3+}/Mn^{4+}$. Additionally, possible MNZ degradation pathways were identified through UPLC-QTOF/MS analysis. Consequently, this study accomplished the development of highly stable, environmentally friendly, and efficient catalysts for PMS activation with lower metal leaching, thereby offering a promising method for effectively removing persistent organic pollutants from real-world water sources.

Received 23rd March 2026
Accepted 26th May 2026

DOI: 10.1039/d6ra02369j

rsc.li/rsc-advances

Open Access Article. Published on 02 June 2026. Downloaded on 6/17/2026 12:25:31 AM.
This article is licensed under a Creative Commons Attribution-NonCommercial 3.0 Unported Licence.

1. Introduction

Antibiotic residues in water systems are a global public health issue that has emerged in recent years, as they introduce the risk of the development of antibiotic resistance among microbes and possibly lead to serious health hazards.[1–3] The global health crisis is worsened by the indiscriminate discharge of agricultural and industrial pollutants, such as pesticides, organic pigments, and pharmaceutical byproducts, into water. Metronidazole (MNZ), a prominent nitroimidazole antibiotic, possesses both antibacterial and anti-inflammatory properties.[4,5] Owing to its high water solubility and lower molecular weight, MNZ can penetrate microbial cell membranes, where it is reduced, potentially resulting in damage to microbial DNA.[6] The chemical structure of MNZ features a five-membered heterocyclic ring linked to a nitro group that contributes to the structure's stability, thereby complicating its removal *via* standard water treatment processes.[7] As a result, the environment has been subject to considerable MNZ contamination, which negatively affects the health of both humans and animals by promoting microbial development and reproduction.[8,9] Consequently, it is imperative to devise a viable approach for the degradation of the MNZ antibiotic in the aqueous environment.[10]

In recent years, there has been significant research interest in electrocatalysis, photocatalysis, heterogeneous catalysis,

[a]*Department of Chemistry, Rahim Yar Khan Campus, The Islamia University of Bahawalpur, Rahim Yar Khan 64200, Pakistan. E-mail: Muhammad.aadil@iub.edu.pk*
[b]*School of Chemical Engineering, Yeungnam University, 280 Daehak-ro, Gyeongsan, Gyeongbuk, 38541, Republic of Korea*
[c]*Department of Materials Engineering, NED University of Engineering and Technology Karachi, Pakistan*
[d]*Department of Physics, College of Science, Imam Mohammad Ibn Saud Islamic University (IMSIU), Riyadh, 11623, Saudi Arabia*
[e]*Department of Physics, Faculty of Science, Islamic University of Madinah, Madinah, 42351, Saudi Arabia*
[f]*Department of Chemistry, College of Science, Qassim University, Buraydah, 51452, Saudi Arabia*
[g]*Department of Physics, College of Science, Princess Nourah bint Abdulrahman University, P.O. Box 84428, Riyadh, 11671, Saudi Arabia*
[h]*Department of Science and Technology, University College at Nairiyah, University of Hafr Al Batin (UHB), Nairiyah, 31981, Saudi Arabia*
[i]*Chemical Engineering Department, College of Engineering, University of Ha'il, P.O. Box 2440, Ha'il, 81441, Saudi Arabia*
† equal contributions.

Open Access Article. Published on 02 June 2026. Downloaded on 6/17/2026 12:25:31 AM. This article is licensed under a Creative Commons Attribution-NonCommercial 3.0 Unported Licence.

adsorption, membrane filtration and advanced oxidation processes for elimination of toxic organic pollutants from aqueous solutions.[11,12] Advanced oxidation processes utilizing peroxymonosulfate (PMS) activation can be designed to degrade antibiotics *via* the generation of superoxide ($O_2^{\bullet-}$), hydroxyl ($^{\bullet}OH$), and sulfate ($SO_4^{\bullet-}$) radicals, as well as non-radical singlet oxygen ($^1O_2$).[13,14] The $SO_4^{\bullet-}$ radical demonstrates a broader pH range (2–9) responsiveness, and a larger reduction potential (2.5–3.0 V) in contrast to the $^{\bullet}OH$ radical.[15] Various procedures have been employed to induce PMS to generate $SO_4^{\bullet-}$, including UV light, heat, ultrasonication, carbonaceous materials, and transition metals.[16]

Practical implementations in environmental areas necessitate the advancement of strong catalysts for the elimination of antibiotics. Nevertheless, the aggregation of catalyst material resulted in a reduction in its surface area, which in turn impeded catalyst activity and increased energy consumption and PMS.[17] Recently, the utilization of transition metal-based catalysts to activate PMS is considered a promising approach.[18,19] Their use is mainly preferred due to their operational simplicity, low energy needs, the reduction of pollutants, and their widespread availability.[20] However, the leaching of metal ions during the catalytic process is a common problem for certain catalysts, such as manganese, iron, nickel, and cobalt.[21] The process of leaching can lead to secondary pollution and potential health risks, which limits the practical use of these materials in water treatment.[22] Therefore, creating catalysts that are structurally stable, maintain high activity for a long time, and have a minimal environmental impact remains a significant challenge.

Manganese-based materials, particularly manganese oxides (Mn_3O_4), are highly valued among transition metal-based activators because they are abundant, eco-friendly, low-cost, have mixed-valence chemistry, and are stable in the environment.[23] Mn_3O_4 is known for its inherent stability, which is a result of its unique distorted spinel structure. This structure consists of manganese ions in two different oxidation states, Mn^{2+} species that occupy the tetrahedral sites, and Mn^{3+} species that occupy octahedral sites.[24] Such a long-range ordered distribution of Mn^{2+} and Mn^{3+} ions could be beneficial for PMS activation.[25] So, the Mn_3O_4/PMS system has shown significant efficiency in the degradation of organic pollutants.[26] Despite showing exceptional PMS activation catalytic activity, the agglomeration of Mn_3O_4 nanoparticles due to their poor thermal and chemical stabilities hindered reproducibility.[27] Simultaneously, the retrieval of the particulate catalyst without the presence of a carrier is not only a complex process, but it is also difficult to avoid the continuous leaching of the nanoparticles into the environment.[28] Carbonaceous materials have been extensively employed as the matrix for Mn_3O_4-based materials to enhance their stability and conductivity in order to address these obstacles.[29]

Biochar, a carbonaceous porous substance, presents an attractive combination of affordability, sustainability *via* waste valorization, elevated specific surface area, and easily alterable surface chemistry.[30–32] Biochar is formed through the pyrolysis of biomass under oxygen-limited or anoxic conditions at high temperatures.[33] It can be widely employed as a catalyst support due to its environmental friendliness and benefit for the PMS activation process.[34] Nonetheless, the catalytic efficacy of unmodified biochar often proves inadequate for PMS activation due to its chemical inertness.[35] Therefore, initiatives to improve its performance are being aggressively implemented to realize its full potential as an effective catalyst. Combining transition metal oxides with biochar has shown promise in creating complex structures with many active sites, which could help activate PMS.[36]

Based on the exceptional catalytic properties of Mn_3O_4 and biochar as a supporting material, we have developed highly efficient Mn_3O_4/biochar through hydrothermal and co-precipitation methods. Mn_3O_4/biochar was used to trigger PMS and, thus, exploited for the elimination of the MNZ antibiotic from wastewater. The surface morphology, crystallinity, surface chemistry, and other features of the produced Mn_3O_4/biochar catalyst were determined through a diverse characterization technique. Mn_3O_4/biochar's catalytic competence was further examined by MNZ degradation under varied circumstances. Additionally, the mitigation of MNZ in the presence of ionic species, naturally occurring organic matter, and various water systems using Mn_3O_4/biochar catalyst was examined. The identification of ROS was accomplished through radical scavenging experiments and a plausible degradation method was deduced based on the intermediate products. Finally, the interaction between the Mn_3O_4/biochar and PMS along with the elimination of contaminants has been lavishly explained by this study.

2. Experimental

2.1. Chemicals

$KMnO_4$, polyethylene glycol (PEG), sodium hydroxide (NaOH), potassium peroxymonosulfate ($2KHSO_5$ $KHSO_4$ K_2SO_4), metronidazole ($C_6H_9N_3O_3$), HNO_3, NaCl, $NaNO_3$, $NaHCO_3$, humic acid, CH_3OH, C_2H_5OH, and *tert*-butyl alcohol ($C_4H_{10}O$), L-histidine ($C_6H_9N_3O_2$), were purchased from Sigma Aldrich. Throughout the experiments, deionized water was used for sample preparation and catalytic activity evaluation.

2.2. Synthesis of Mn_3O_4/biochar

In this investigation, wheat straw was chosen as the standard lignocellulosic biomass due to its cost-effectiveness and global availability for biochar production. The biochar was synthesized through the pyrolysis of wheat straw in a tubular furnace at 500 °C with a heating rate of 5 °C min^{-1} for 180 minutes under a nitrogen atmosphere.

For the preparation of Mn_3O_4, $KMnO_4$ (0.79 g) was solubilized in water (30 mL) under continuous agitation to homogenize the mixture. Then, introduce 30 mL of PEG to the $KMnO_4$ solution and continue agitation for an additional 30 minutes. The processed mixture was taken in a 100 mL Teflon-lined autoclave which was maintained at 120 °C for 10 h. When cooled, the reddish-brown Mn_3O_4 was vacuum filtered and washed several times alternately with ethanol and deionized

 © 2026 The Author(s). Published by the Royal Society of Chemistry

Open Access Article. Published on 02 June 2026. Downloaded on 6/17/2026 12:25:31 AM.
This article is licensed under a Creative Commons Attribution-NonCommercial 3.0 Unported Licence.

water. Ultimately, the powdered material was heated to 50 °C and desiccated in a dehydrating oven for 10 hours. The final sample was then named Mn_3O_4.

Subsequently, the Mn_3O_4/biochar composite was synthesized *via* a simple chemical coprecipitation method. Initially, biochar (0.5 g) was dispersed in C_2H_5OH (50 mL) for a duration of five minutes to form suspension A. Concurrently, suspension B was obtained by dispersing Mn_3O_4 (1 g) powder in water (50 mL) for one hour. Following this, suspensions A and B were amalgamated and subjected to magnetic stirring for a period of two hours. Following vacuum filtering, the as-synthesized Mn_3O_4/biochar composites were dried at 70 °C for half a day. The mass ratio of Mn_3O_4 to biochar for the synthesis of Mn_3O_4/biochar was 2 : 1 (1 g Mn_3O_4 and 0.5 g biochar), corresponding to about 33 wt% biochar in the composite.

2.3. Catalytic evaluation of Mn_3O_4/biochar

To analyze the catalytic performance of prepared catalysts, MNZ, a common antibiotic, was considered as a probe, and the degradation was performed using PMS. The experimental process was accomplished in a flask, containing 100 mL of MNZ solution (30 mg L^{-1}) and a catalyst concentration of 0.45 g L^{-1} at room temperature and with continuous stirring. Later on, the reaction mixture was kept for $\frac{1}{2}$ h to facilitate sorption equilibrium. The degradation process of MNZ was initiated by incorporating the PMS (0.24 mM) to the reaction mixture. During degradation reactions, the pH was adjusted by introducing 1.0 M solutions of NaOH and HNO_3. After taking 0.5 mL samples of the mixture at different times during the degradation, the reaction was stopped by adding an equal amount of methanol. The resulting mixture was subsequently filtered using PTFE filters (pores = 0.22 μm). HPLC was implemented to measure the residual MNZ. The degradation of MNZ was affected by several factors: the amount of PMS used (0, 0.08, 0.16, 0.24, and 0.32 mM), the concentration of the catalyst (0.0, 0.15, 0.30, 0.45, and 0.60 g L^{-1}), the initial concentration of MNZ (10, 20, 30, 40, and 50 mg L^{-1}), and the pH of the solution (3, 4.86 (unadjusted), 7, 9, and 11). In addition, the effects of ionic species and natural organic molecules on MNZ decomposition were studied to assess the catalyst's potential for treating real wastewater. Furthermore, radical quenching studies were carried out to determine the major reactive oxygen species (ROS) in MNZ degradation. Scavengers were introduced at the beginning of the process with the concentrations as follows: methanol (100 mM) and *tert*-butyl alcohol (TBA, 100 mM) for $^{\bullet}OH/SO_4^{\bullet-}$ and $^{\bullet}OH$ respectively, while L-histidine (10 mM) for $^1O_2$.

3. Results and discussion

3.1. Catalyst characterizations

As illustrated in Fig. 1, XRD study was conducted to investigate the lattice structure and crystal phase purity of Mn_3O_4, biochar, and Mn_3O_4/biochar. From Fig. 1, it is clear that pristine Mn_3O_4 unveiled distinctive diffraction peaks at 18.08°, 28.96°, 31.18°, 32.42°, 36.21°, 38.21°, 44.65°, 50.82°, 53.96°, 56.17°, 58.60°, 60.07°, and 64.88°. The observed peaks correspond to the (101), (112), (200), (103), (211), (004), (220), (105), (312), (303), (321), (224), and (400) planes, respectively, confirming the formation of highly crystalline tetragonal hausmannite Mn_3O_4 (JCPDS no. 24–0734) with an $I4_1/amd$ space group characterized by mixed Mn^{2+}/Mn^{3+} valence states.[37,38] On the other hand, the diffraction peaks ranging from 21.83° to 24.3° in the XRD spectra of biochar were related to the (002) plane of amorphous carbon,[39] while the peak at 26.58° was related to the (111) plane of graphitic-carbon.[40] The successful formation of Mn_3O_4/biochar composites is confirmed by the presence of all characteristic planes of both Mn_3O_4 and biochar in the XRD spectra. However, the peak intensity of biochar in Mn_3O_4/biochar composites exhibited a marked reduction when compared to the pure biochar, which can be attributed to their comparatively low concentration within the composite structure.

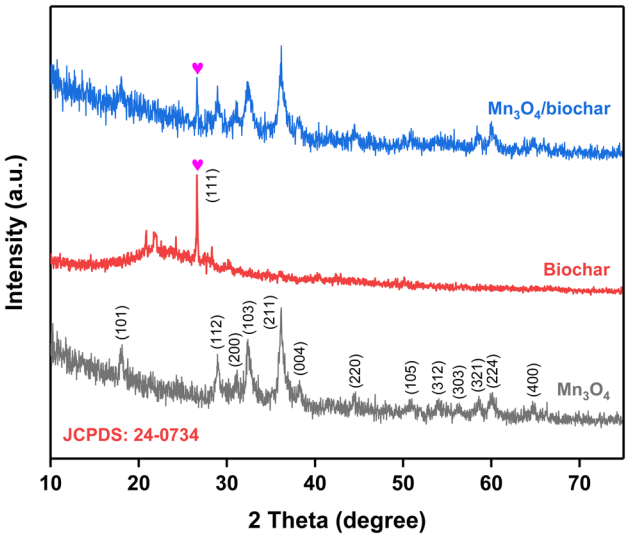

Fig. 1 XRD spectrum of Mn_3O_4, biochar, and Mn_3O_4/biochar.

SEM was used to examine the shape and structure of Mn_3O_4/biochar. The SEM micrographs in Fig. 2(a–c) illustrate the surface topography of the synthesized Mn_3O_4/biochar composite at different magnifications. The Mn_3O_4 phase shows anisotropic crystal growth and is characterized by small and particle-like crystals that are combined with biochar. The biochar surface has effectively immobilized the heterogeneous distribution of Mn_3O_4 particles, resulting in a multi-phase composite of a carbon matrix and metal oxide particles. Furthermore, SEM-EDS elemental mapping analysis verifies the effective formation of the Mn_3O_4/biochar composite. Fig. 2(d–g) indicates that the composite surface was distributed with C, O, and Mn. This suggests that Mn_3O_4 was deposited onto the biochar material.

The elemental makeup is substantiated by the EDS spectrum (Fig. 2(h)), which displays prominent peaks associated with C, O, and Mn, specifically with weight percentages of 26.4% for C, 20.4% for O, and 53.2% for Mn. The elevated concentrations of Mn and O, alongside a suitable C content, suggest that Mn_3O_4 particles are effectively anchored to the biochar surface, rather than being present as a distinct phase. As a result, the

Open Access Article. Published on 02 June 2026. Downloaded on 6/17/2026 12:25:31 AM.
This article is licensed under a Creative Commons Attribution-NonCommercial 3.0 Unported Licence.

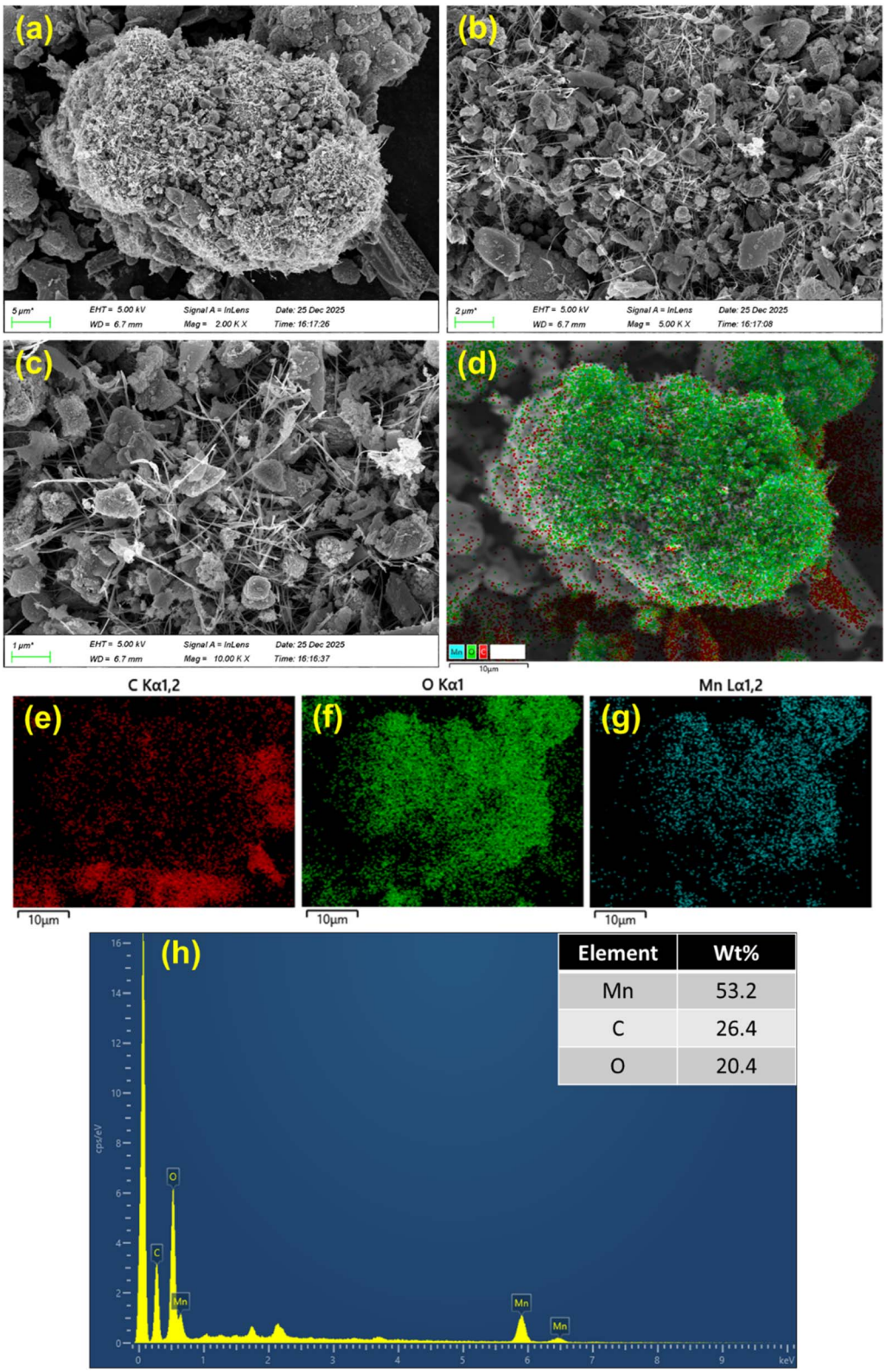

Fig. 2 (a–c) SEM micrographs of Mn_3O_4/biochar at different magnifications, (d–g) EDS mapping and (h) EDS quantitative analysis (inset representing the weight percentages) of Mn_3O_4/biochar.

consistent distribution of all three elements, absent of substantial impurities, confirms the successful fabrication of the Mn_3O_4/biochar composite.

The surface chemical makeup and the changes in valence states of Mn_3O_4/biochar were interpreted through XPS study. The comprehensive scan spectrum of Mn_3O_4/biochar shown in

© 2026 The Author(s). Published by the Royal Society of Chemistry

Open Access Article. Published on 02 June 2026. Downloaded on 6/17/2026 12:25:31 AM.
This article is licensed under a Creative Commons Attribution-NonCommercial 3.0 Unported Licence.

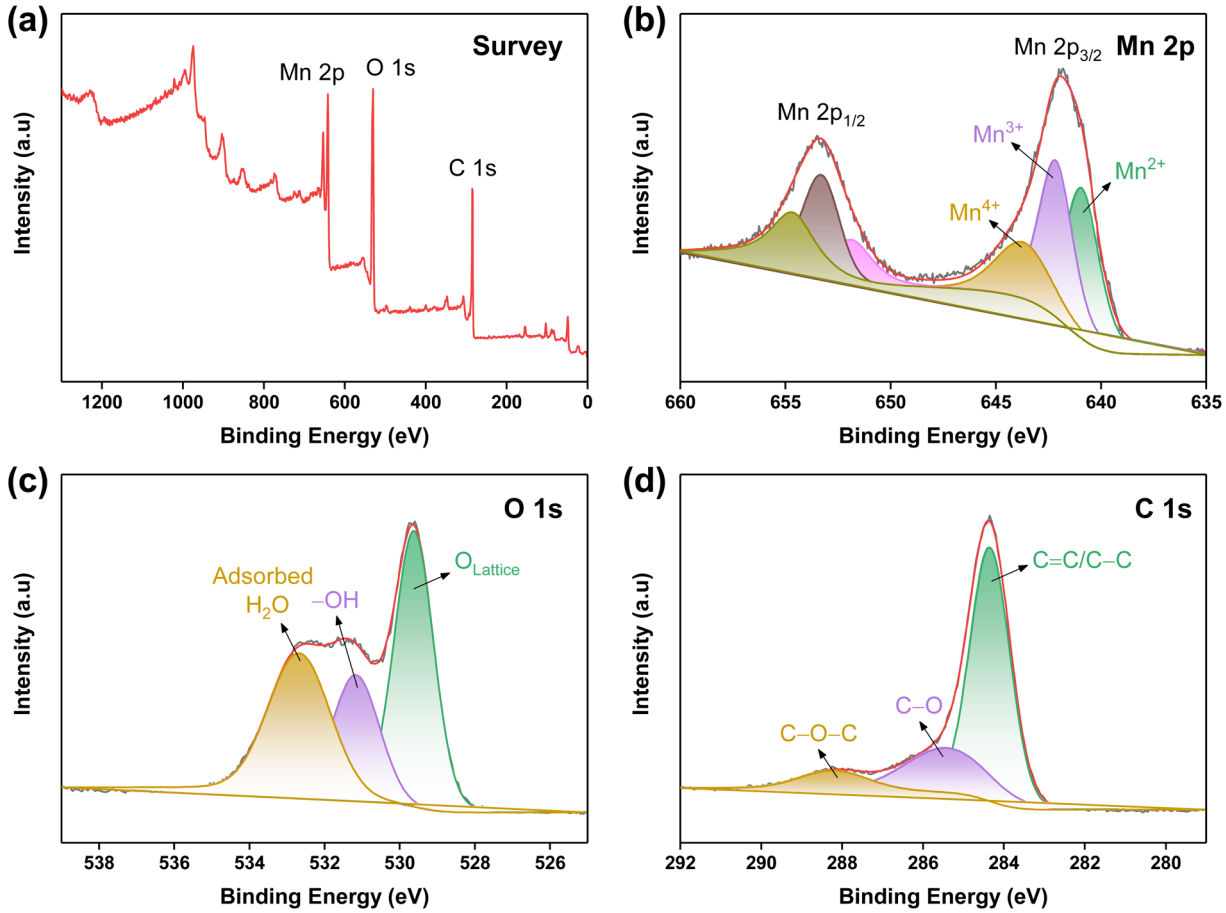

Fig. 3 XPS spectral analysis of Mn_3O_4/biochar; (a) survey scan, (b) Mn 2p, (c) O 1s, (d) C 1s.

Fig. 3(a)) validated the existence of O, Mn, and C in the composite sample. The Mn 2p spectrum (Fig. 3(b)) displayed two main peaks, Mn $2p_{3/2}$ and Mn $2p_{1/2}$, at 641.84 eV and 653.42 eV. The difference in spin–orbit binding energy between these peaks was found to be 11.58 eV, which is consistent with previous research on Mn_3O_4. (ref. 41) In addition, the Mn $2p_{3/2}$ peak could be divided into distinct spikes at 641.02, 642.24, and 643.81 eV, related to Mn^{2+}, Mn^{3+}, and Mn^{4+}, separately.[42] The O 1s spectra of the Mn_3O_4/biochar catalyst shown in Fig. 3(c) and its deconvolution yielded three spikes at 529.62, 531.16, and

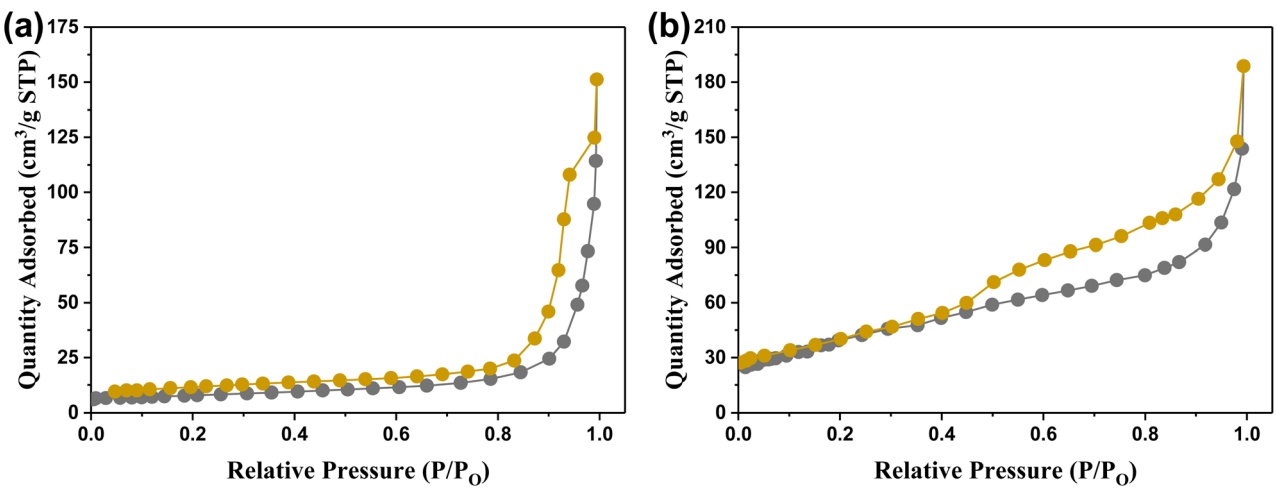

Fig. 4 N_2 adsorption/desorption curves of (a) Mn_3O_4 and (b) Mn_3O_4/biochar.

Open Access Article. Published on 02 June 2026. Downloaded on 6/17/2026 12:25:31 AM. This article is licensed under a Creative Commons Attribution-NonCommercial 3.0 Unported Licence.

532.71 eV, which are ascribed to lattice oxygen, –OH, and adsorbed H_2O species, respectively.[43] The –OH species on the catalyst surface serve as active sites for bond formation with PMS.[44] The C 1s spectra (Fig. 3(d)) showed peaks at 284.36, 285.45, and 288.27 eV. These peaks were accompanied by C=C/C–C, C–O, and C–O–C functional groups, respectively.[45]

The active sites' population on a catalyst's surface is strongly related to its surface area. Fig. 4(a and b) illustrates the adsorption–desorption curves of N_2 for bare Mn_3O_4 and Mn_3O_4/biochar. The BET analysis of both Mn_3O_4 and Mn_3O_4/biochar revealed type IV isotherms, which implies that both materials were typical mesoporous substances.[46,47] The Mn_3O_4/biochar composite established a larger surface area (67.82 m^2 g^{-1}) in contrast to the bare Mn_3O_4 (45.29 m^2 g^{-1}), thus offering a greater density of active sites and facilitating the removal of organic pollutants. The observed increase in the surface area of Mn_3O_4/biochar validated the successful integration of Mn_3O_4 with biochar to form a composite material. The Mn_3O_4/biochar composite is expected to speed up the degradation process and help in the adsorption of pollutant molecules due to its mesoporous structure and larger surface area.

3.2. Performance of Mn_3O_4/biochar for the degradation of MNZ antibiotic

The adsorption removal of MNZ was evaluated to study an interesting relationship between the adsorption performance and catalytic efficiency, as shown in Fig. 5(a). The results indicate that the adsorptive removal of MNZ was quite limited in the presence of various catalysts and reached 7.92% for Mn_3O_4/biochar/PMS, 6.71% for Mn_3O_4/biochar, 5.36% for Mn_3O_4/PMS, 4.32% for Mn_3O_4, and 2.92% for biochar after 30 min of adsorption. Furthermore, the degradation potential of the synthesized Mn_3O_4, biochar, and Mn_3O_4/biochar catalysts was gauged with and without PMS (Fig. 5(b)). Without the presence of any catalyst, the effective removal of MNZ presents a significant challenge, as demonstrated by the negligible (2.65%) reduction in its concentration observed over the 30 minute reaction period, implying that PMS alone could not degrade MNZ. Similarly, the degradation of MNZ was limited to 5.39%, 13.89%, and 23.24% during the same period when biochar, Mn_3O_4, and Mn_3O_4/biochar were utilized in the absence of PMS. The Mn_3O_4/PMS system, however, significantly enhanced the elimination of MNZ and led to the abatement of 74.09% of MNZ in a 30 minute reaction. On the other hand, the utilization of Mn_3O_4/biochar/PMS system as an efficient PMS activator markedly promoted the MNZ elimination, with a complete degradation, within 30 minutes. It was due to the fact that the transition of $Mn^{2+}/Mn^{3+}/Mn^{4+}$ resulted in the activation of PMS to yield highly ROS for the abatement of MNZ.

The kinetic investigation of the specified catalytic systems for MNZ degradation was performed employing the Langmuir–Hinshelwood model, as represented by eqn (1).[48]

$$-\ln\left(\frac{C}{C_0}\right) = k_{app} \cdot t \quad (1)$$

Here, k_{app} signifies the apparent rate constant, while C_0 and C refer to the MNZ initial and final concentrations at time t, respectively. As depicted in Fig. 5(c), the various catalyst systems for MNZ removal exhibited pseudo-first-order kinetics. Fig. 5(d) presents the k_{app} values for MNZ degradation, which were determined to be 0.1402, 0.047, 0.0084, 0.005, and 0.0016 min^{-1}

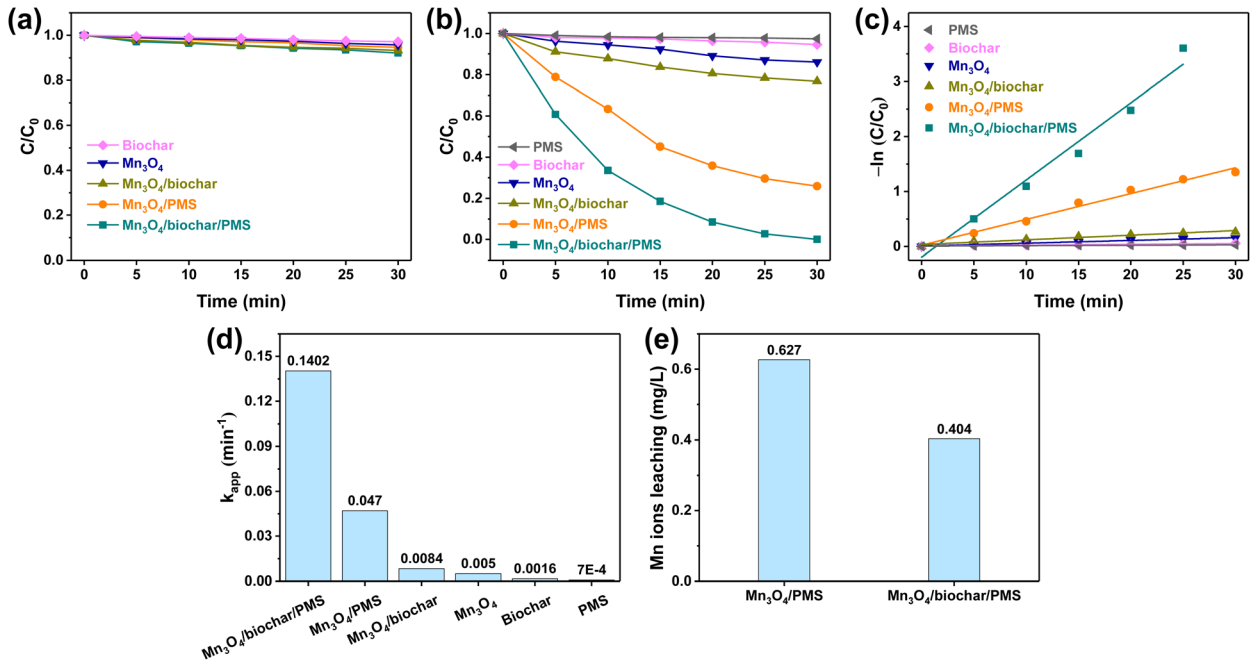

Fig. 5 a) MNZ adsorption in the presence of various reaction systems, (b) MNZ degradation rates in the presence of various reaction systems, (c) study of kinetics, (d) corresponding k_{app}, and (e) Mn ions leaching in Mn_3O_4/PMS and Mn_3O_4/biochar/PMS systems. (Parameters: catalyst = 0.45 g L; PMS = 0.24 mM; MNZ = 30 mg L; pH = 4.86).

© 2026 The Author(s). Published by the Royal Society of Chemistry

Open Access Article. Published on 02 June 2026. Downloaded on 6/17/2026 12:25:31 AM. This article is licensed under a Creative Commons Attribution-NonCommercial 3.0 Unported Licence.

Table 1 Catalytic superiority of Mn_3O_4/biochar over previously reported catalysts for PMS activation towards the degradation of MNZ antibiotics

Catalyst	Synthesis	Pollutant	Degradation	Reaction time	Ref.
NSC-Co_3O_4	Solvothermal/pyrolysis	MNZ	99%	30 min	49
Fe-Ce@N-BC	Hydrothermal	MNZ	97.5%	60 min	50
NiFePx	Phosphorization	MNZ	94.5%	60 min	51
$FeCo_2O_4$-Fe_3O_4	Sol–gel	MNZ	96.8%	60 min	52
Co-MBC	Impregnation pyrolysis	MNZ	90%	60 min	53
$LaCo_{0.8}Mn_{0.2}O_3$	Sol–gel	MNZ	99.42%	30 min	54
C-MCED/Fe(III)	—	MNZ	94.05%	210 min	55
$CoAl_2O_4$@AP	*In situ* growth/calcination	MNZ	97%	100 min	56
Fe/Mn–BC	—	MNZ	94.3%	120 min	57
Mn_3O_4/biochar	Hydrothermal/co-precipitation	MNZ	100%	30 min	This study

for the Mn_3O_4/biochar/PMS, Mn_3O_4/PMS, Mn_3O_4/biochar, Mn_3O_4, and biochar, respectively. The k_{app} of the Mn_3O_4/biochar/PMS system was 2.98 times larger than Mn_3O_4/PMS, indicating that the Mn_3O_4/biochar/PMS system demonstrated a superior degrading capacity. The enhanced MNZ degradation is attributable to the beneficial characteristics and augmented surface area of Mn_3O_4/biochar in facilitating PMS activation. Furthermore, to highlight the importance of our synthesized catalyst, a comparison was made between the catalytic effectiveness of Mn_3O_4/biochar and that of previously researched catalysts (Table 1).

The release of Mn ions was assessed in leaching experiments, which were performed under optimal reaction conditions to determine the practical utility of Mn_3O_4 and Mn_3O_4/biochar catalysts during PMS activation (Fig. 5(e)). The concentrations of leaked Mn ions were measured, yielding values of 0.627 and 0.404 mg L^{-1} for Mn_3O_4/PMS and Mn_3O_4/biochar/PMS systems, respectively. These values are significantly lower than the permitted discharge limit (GB 3838–2002, 1.0 mg L^{-1}),[58] indicating that the synthesized catalysts are suitable for their intended use. Additionally, the leaching results verified that the improved efficiency of Mn_3O_4/biochar was a consequence of the composite formation, which led to a decrease in metal ion leaching.

3.3. Optimization of interfering factors

3.3.1. Influence of Mn_3O_4/biochar loading. To understand the effectiveness of MNZ removal using the Mn_3O_4/biochar/PMS system under the influence of various catalyst loadings, we did degradation experiments with different amounts of catalyst in the range of 0 to 0.60 g L^{-1}. The elimination of MNZ enlarged from 57.62% to complete degradation as the catalyst loading was increased from 0.15 to 0.45 g L^{-1} (Fig. 6(a)). The k_{app} for MNZ elimination was around 0.0295, 0.0716, and 0.1402 min^{-1} at catalyst loadings of 0.15, 0.30, and 0.45, respectively (Fig. 6(b)). The enhanced MNZ abatement efficiency at 0.45 g L^{-1} resulted from the accessibility of supplementary active sites for PMS stimulation, which contributed to the rise in mitigation rate as catalyst loading was raised.[59] Conversely, the MNZ mineralization efficacy experienced a slight decrease, reaching 97.07%, at a catalyst dosage of 0.60 g L^{-1}. Furthermore, the k_{app} value was correspondingly reduced to 0.1188 min^{-1}. The quenching of free radicals may be attributed to the recombination of surplus radicals or the self-aggregation of excess catalysts, which could explain the decrease in degradation efficacy.[60]

3.3.2. Influence of PMS quantity. To determine the influence of PMS conc. on the effectiveness of MNZ elimination in the Mn_3O_4/biochar/PMS system, trials were performed using different PMS amounts (Fig. 6(c)). Evidently, increasing the con. of PMS markedly improved the effectiveness of MNZ removal. The MNZ abatement proficiency was substantially enhanced from 48.16% to complete degradation as the PMS dosage enlarged from 0.08 to 0.24 mM, while the k_{app} enlarged from 0.0215 to 0.1402 min^{-1} (Fig. 6(d)). By contrast, a slight reduction in removal efficiency to 95.58% was recorded, with a k_{app} of 0.1038 min^{-1}, upon increasing the PMS concentration to 0.32 mM. These observations can be explained by two key factors: (i) the Mn_3O_4/biochar catalyst demonstrated an enhanced capacity to activate PMS, thereby generating a greater quantity of ROS, which, in turn, accelerated the elimination of MNZ when the PMS concentration was at 0.24 mM. (ii) Simultaneously, the surplus PMS may have interacted with the excess $SO_4^{\bullet-}$ radical,[61] consequently producing less ROS, causing a decline in decomposition efficacy as the PMS concentration surpassed 0.32 mM. Subsequently, the reasonable quantity of PMS for successive trials was determined to be 0.24 mM.

3.3.3. Influence of MNZ concentration. The consequence of the MNZ quantity on the degradation process was investigated, and the obtained results for different MNZ con (Fig. 6(e)). The degrading efficacy was adversely affected by the increase in MNZ initial concentration. In fact, the abatement of MNZ was more facilitated by lower initial concentrations. At 10 mg L^{-1}, MNZ can be completely degraded in 25 min, while at 20 and 30 mg L^{-1}, complete degradation is achieved in 30 min. Similarly, the observed k_{app} values for MNZ degradation decreased significantly, from 0.1598 min^{-1} to 0.0825 min^{-1}, as the MNZ amount amplified from 10 to 50 mg L^{-1} (Fig. 6(f)). The explanation may be further emphasized by the fact that the number of ROS was restricted as a result of the limited availability of PMS and catalyst.[62] Therefore, the degradation efficacy may be reduced as a result of the competition for ROS in the reaction system, which is caused by the increase in MNZ molecules.

Open Access Article. Published on 02 June 2026. Downloaded on 6/17/2026 12:25:31 AM.
This article is licensed under a Creative Commons Attribution-NonCommercial 3.0 Unported Licence.

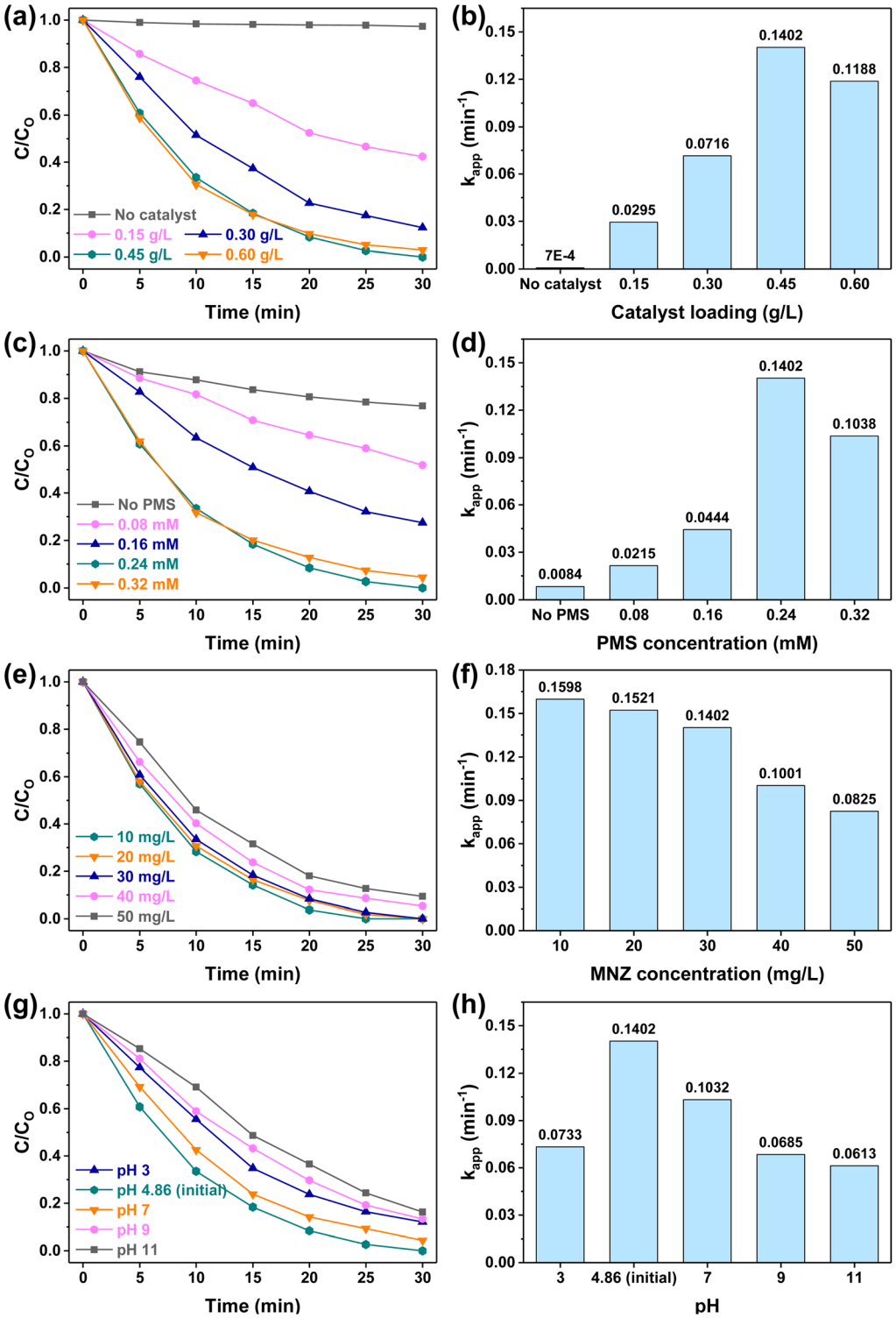

Fig. 6 MNZ degradation under the influence of (a and b) Mn_3O_4/biochar loading, (c and d) PMS quantity, (e and f) MNZ concentration, and (g and h) pH using the Mn_3O_4/biochar/PMS system.

3.3.4. Influence of the pH. The influence of the pH of the solution is another critical aspect that alters the surface belongings of the catalyst and controls the active species generation.[63] Therefore, the trials were performed over a pH assortment of 3–11 to investigate the impact of pH on the decomposition of MNZ using the Mn_3O_4/biochar/PMS, as shown in Fig. 6(g). The outcomes indicated that MNZ mitigation was more efficient under slightly acidic and neutral conditions. The Mn_3O_4/biochar/PMS system achieved complete MNZ removal at pH 4.86 (unadjusted initial pH), thereby showcasing

© 2026 The Author(s). Published by the Royal Society of Chemistry

Open Access Article. Published on 02 June 2026. Downloaded on 6/17/2026 12:25:31 AM. This article is licensed under a Creative Commons Attribution-NonCommercial 3.0 Unported Licence.

its high MNZ degradation capability. Furthermore, even at pH 7, MNZ degradation was still substantial, reaching 95.57%, which highlights the catalyst's broad applicability across a range of pH levels. Conversely, MNZ degradation was limited to 87.85%, 86.59%, and 83.72% at pH 3, 9, and 11, respectively. The k_{app} for pH 3, 4.86, 7, 9, and 11 were 0.0733, 0.1402, 0.1032, 0.0685, and 0.0613 min^{-1}, separately (Fig. 6(h)). At pH 4.86, the elevated k_{app} value of 0.1402 min^{-1} correlates with the most significant degree of MNZ elimination. Because of the rise in H^+ concentration at pH 3, the interface among PMS and MNZ, which may boost the establishment of H-bonding *via* the H^+ and HSO_5^-, is repressed under very acidic circumstances.[64] Additionally, as seen in eqn (2) and (3), H^+ may reduce the effectiveness of MNZ degradation by quenching $SO_4^{\bullet-}$ and $^{\bullet}OH$.

$$H^+ + SO_4^{\bullet-} + e^- \rightarrow HSO_4^{\bullet-} \quad (2)$$

$$H^+ + {}^{\bullet}OH + e^- \rightarrow H_2O \quad (3)$$

It is also important to note that in basic conditions, the reaction among $SO_4^{\bullet-}$ and $H_2O/^-OH$ might produce $^{\bullet}OH$ (eqn (4) and (5)), which has a reduced redox potential, causing the degradation ineffectiveness.

$$SO_4^{\bullet-} + H_2O \rightarrow SO_4^{2-} + {}^{\bullet}OH + H^+ \quad (4)$$

$$SO_4^{\bullet-} + {-}OH \rightarrow SO_4^{2-} + {}^{\bullet}OH \quad (5)$$

3.3.5. Influence of coexisting anions. A variety of inorganic ions and HA have been demonstrated to effectively quench the ROS generated through the PMS activation, and the incidence of such specific ions in water may impact the efficiency of the Mn_3O_4/biochar. Numerous inorganic ions have been seen to rapidly quench the reactive radicals. The presence of such ions may significantly influence the catalyst's ability. The impact of these ions on the MNZ abatement *via* Mn_3O_4/biochar catalyst is seen in Fig. 7. The data in Fig. 7(a) demonstrate that 10 mM Cl^- somewhat obstructs the removal rate of MNZ, reducing it to 92.41%. Cl^- can quickly undergo a reaction with $SO_4^{\bullet-}$ or $^{\bullet}OH$ radicals produced by the Mn_3O_4/biochar catalyst through PMS activation. This reaction leads to the generation of chlorinated radicals ($Cl_2^{\bullet-}$), which have a lower oxidation potential, thereby decreasing the degradation efficiency of MNZ (eqn (6)–(9)).[65]

$$SO_4^{\bullet-} + Cl^- \rightarrow SO_4^{2-} + Cl^{\bullet} \quad (6)$$

$$Cl^- + {}^{\bullet}OH \rightarrow ClOH^{\bullet} \quad (7)$$

$$ClOH^{\bullet} + H^+ \rightarrow Cl^{\bullet} + H_2O \quad (8)$$

$$Cl^{\bullet} + Cl^- \rightarrow Cl_2^{\bullet-} \quad (9)$$

Conversely, the introduction of 10 mM NO_3^- only slightly slows down the breakdown of MNZ, reaching 95.67%. This effect may be due to the reaction between NO_3^- and $SO_4^{\bullet-}$, which produces less reactive $NO_3^{\bullet}$ radicals (eqn (10)), thereby hindering the degradation process.

$$NO_3^- + SO_4^{\bullet-} \rightarrow NO_3^{\bullet} + SO_4^{2-} \quad (10)$$

Conversely, the presence of HCO_3^- significantly reduced the degradation of MNZ. Specifically, adding 10 mM HCO_3^- repressed the reduction of MNZ, resulting in a total degradation of 84.52%. This decrease in abatement was ascribed to the interaction between HCO_3^- and $SO_4^{\bullet-}/^{\bullet}OH$, which led to the generation of $HCO_3^{\bullet}$, a species with a lower oxidation potential, thereby hindering effective MNZ degradation (eqn (11) and (12)).[66]

$$HCO_3^- + SO_4^{\bullet-} \rightarrow HCO_3^{\bullet} + SO_4^{2-} \quad (11)$$

$$HCO_3^- + {}^{\bullet}OH \rightarrow CO_3^{\bullet-} + H_2O \quad (12)$$

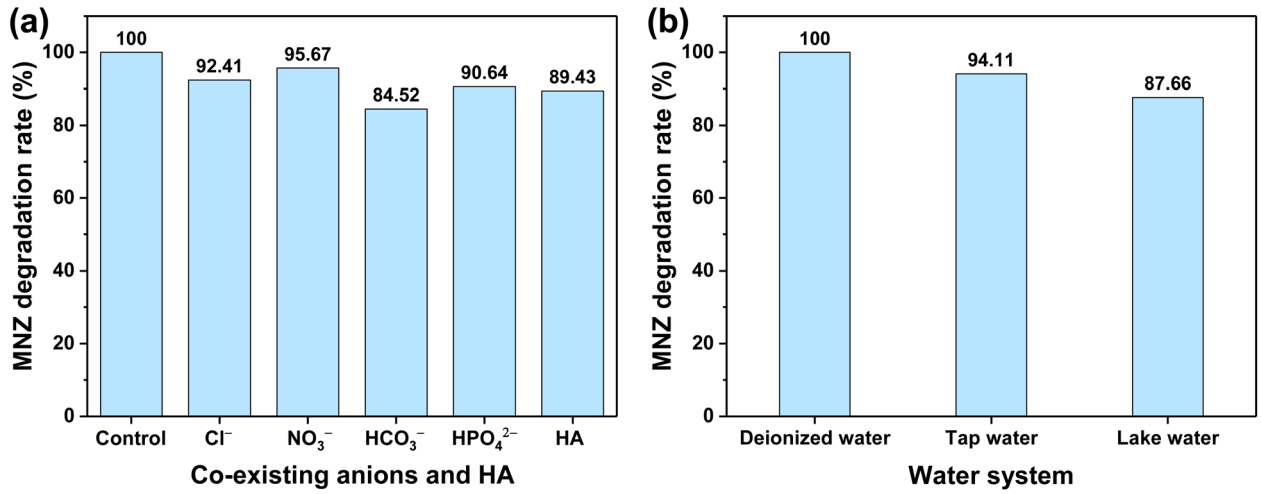

Fig. 7 MNZ degradation under the influence of (a) co-existing anions and HA and (b) different water systems using the Mn_3O_4/biochar/PMS system. (Parameters: Mn_3O_4/biochar = 0.45 g L; PMS = 0.24 mM; MNZ = 30 mg L; pH = 4.86).

Open Access Article. Published on 02 June 2026. Downloaded on 6/17/2026 12:25:31 AM. This article is licensed under a Creative Commons Attribution-NonCommercial 3.0 Unported Licence.

Conversely, the presence of HPO_4^{2-} significantly reduced the effectiveness of MNZ removal to 90.64%. HPO_4^{2-} may react with $SO_4^{\bullet-}$/$^{\bullet}OH$, hence hindering MNZ degradation (eqn (13) and (14)).[67] Furthermore, the crystallization of HPO_4^{2-} with metallic ions could reduce the catalyst's effectiveness in activating PMS.

$$HPO_4^{2-} + SO_4^{\bullet-} \rightarrow HPO_4^{\bullet-} + SO_4^{2-} \quad (13)$$

$$HPO_4^{2-} + {}^{\bullet}OH \rightarrow HPO_4^{\bullet-} + OH^- \quad (14)$$

Moreover, HA, a common redox-active substance, has the potential to hinder MNZ reduction. This occurs through the blockage of the catalyst's active sites and competition for the production of ROS. In accordance with this premise, the MNZ mineralization rate was assessed by adding 20 mg L^{-1} of HA, and the results are presented in Fig. 7(a). The mitigation of MNZ was shown to be a diminution from complete to 89.43% over a 30 minute reaction, thereby indicating that even a modest concentration of HA can substantially hinder MNZ degradation.

To assess the practical utility of the Mn_3O_4/biochar/PMS system in real-world aquatic environments, tap water and artificial lake water served as representative matrices for investigating MNZ removal across diverse water quality conditions. In tap water and lake water, the removal efficiencies of MNZ, as shown in Fig. 7(b), were 94.11% and 87.66%, respectively. This suggests that the system effectively breaks down MNZ under conditions similar to those found in real-world situations. These findings reveal that the Mn_3O_4/biochar/PMS system has definite aptitude for real-world use in wastewater treatment.

3.4. Identification of active species

To identify the predominant ROS produced during the breakdown of MNZ using the Mn_3O_4/biochar/PMS, radical trapping studies were conducted as seen in Fig. 8(a and b). In most PMS-based AOPs, $SO_4^{\bullet-}$/$^{\bullet}OH$ radicals are the main ROS that have been identified. Methanol served as an active quenching agent for $SO_4^{\bullet-}$/$^{\bullet}OH$ radicals. Conversely, *tert*-butyl alcohol (TBA) quickly reacts with $^{\bullet}OH$ radicals.[68] Therefore, methanol and TBA were used as specific indicators for $SO_4^{\bullet-}$/$^{\bullet}OH$ and $^{\bullet}OH$, separately.[69,70] Upon the addition of methanol, the MNZ elimination rate reduced to 44.61%, yielding k_{app} of 0.0193 min^{-1}. Moreover, using the TBA, the degrading efficiency decreased to 55.37%, accompanied by a k_{app} of 0.0272 min^{-1}. These findings demonstrated that $SO_4^{\bullet-}$ and $^{\bullet}OH$ were generated in the Mn_3O_4/biochar/PMS system, with $SO_4^{\bullet-}$ being one of the most predominant radicals. Alongside $SO_4^{\bullet-}$ and $^{\bullet}OH$, other prevalent non-radicals, including $^1O_2$, also played a role in the breakdown of MNZ. Consequently, L-histidine was chosen as a scavenger for $^1O_2$. The removal efficiencies of MNZ, as shown in Fig. 8(a and b), decreased to 91.04% with the addition of L-histidine. This was accompanied by a reduction in k_{app} values to 0.0805 min^{-1}. Therefore, the results from the quenching experiments suggested that $SO_4^{\bullet-}$/$^{\bullet}OH$/$^1O_2$ were the main ROS participating in MNZ removal within the Mn_3O_4/biochar/PMS system.

3.5. Degradation mechanism and pathways

The degradation of MNZ within the Mn_3O_4/biochar/PMS system was postulated, as illustrated in Fig. 9, based on the preceding characterizations and experimental findings. Initially, Mn_3O_4/biochar and PMS were introduced into the MNZ solution. Subsequently, PMS was adsorbed onto the Mn_3O_4/biochar surface *via* electrostatic attraction, initiating a reaction that generated free radicals. Electrons from the oxidation processes of Mn^{2+}/Mn^{3+} and Mn^{3+}/Mn^{4+} produced $SO_4^{\bullet-}$, which activated PMS (eqn (15) and (17)). The oxidation states of Mn (Mn^{3+}/Mn^{4+}) could be transformed into the reductive states of Mn (Mn^{2+}/Mn^{3+}). This resulted in the formation of $SO_5^{\bullet-}$ (eqn (16) and (18)), which was important to enhance the activity of Mn_3O_4 and preserve its stability. In the meantime, the breakdown of MNZ was also linked to the formation of $^{\bullet}OH$ by the interaction of

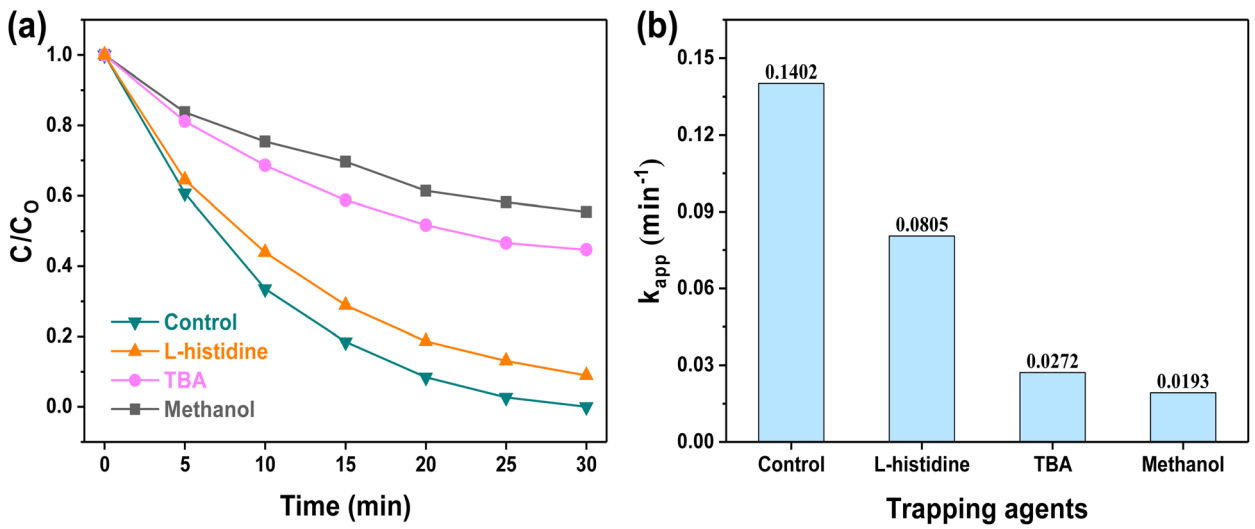

Fig. 8 (a) Radical scavenging experiments for the determination of active species participating in the MNZ abatement using the Mn_3O_4/biochar/PMS system and (b) corresponding k_{app} values. (Parameters: Mn_3O_4/biochar = 0.45 g L; PMS = 0.24 mM; MNZ = 30 mg L; pH = 4.86).

© 2026 The Author(s). Published by the Royal Society of Chemistry

Open Access Article. Published on 02 June 2026. Downloaded on 6/17/2026 12:25:31 AM.
This article is licensed under a Creative Commons Attribution-NonCommercial 3.0 Unported Licence.

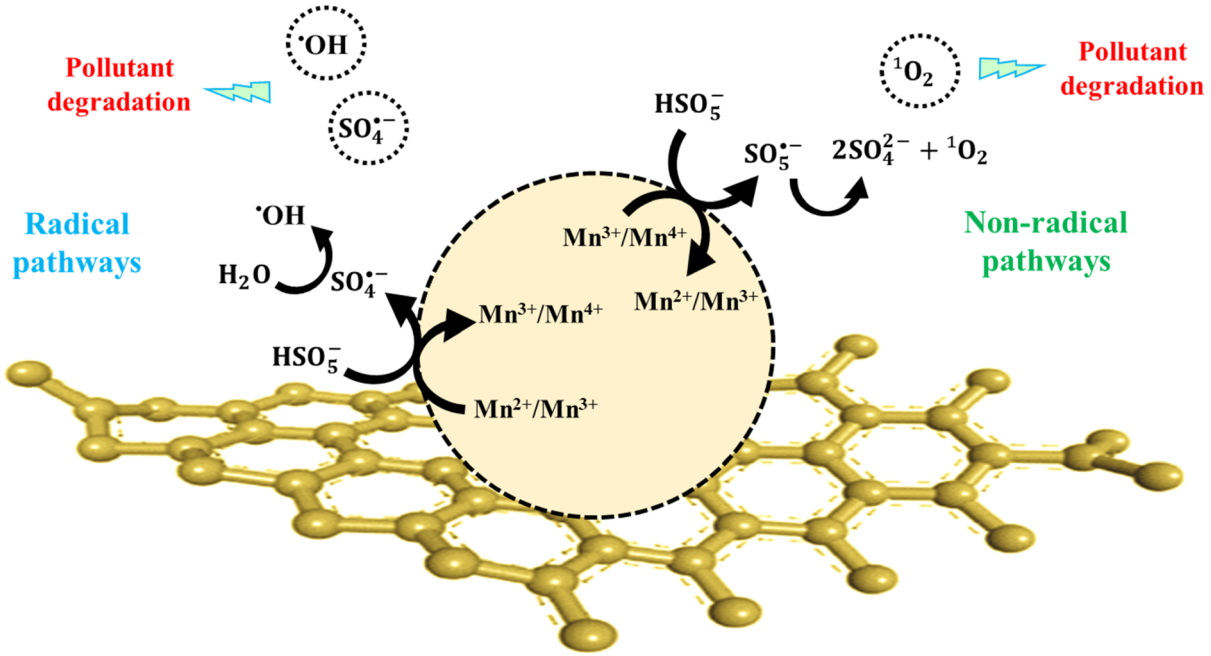

Fig. 9 PMS activation and MNZ degradation mechanism using Mn_3O_4/biochar/PMS.

$SO_4^{\bullet -}$ with H_2O or –OH (eqn (19) and (20)). However, the created $SO_5^{\bullet -}$ would also contend with the –OH, leading to the production of ·OH. Additionally, L-histidine quenching experiments verified the important role of $^1O_2$ in the MNZ abatement. The $SO_5^{\bullet -}$ radical produced may also combine with water or itself to yield $^1O_2$ (eqn (21) and (22)). Ultimately, the generated $SO_4^{\bullet -}$ and ·OH radicals and $^1O_2$ non-radicals can transform MNZ into low molecular weight non-toxic products (eqn (23)).

$$Mn^{2+} + HSO_5^- \rightarrow Mn^{3+} + OH^- + SO_4^{\bullet -} \quad (15)$$

$$Mn^{3+} + HSO_5^- \rightarrow Mn^{2+} + H^+ + SO_5^{\bullet -} \quad (16)$$

$$Mn^{3+} + HSO_5^- \rightarrow Mn^{4+} + OH^- + SO_4^{\bullet -} \quad (17)$$

$$Mn^{4+} + HSO_5^- \rightarrow Mn^{3+} + H^+ + SO_5^{\bullet -} \quad (18)$$

$$SO_4^{\bullet -} + H_2O \rightarrow SO_4^{2-} + H^+ + {}^{\bullet}OH \quad (19)$$

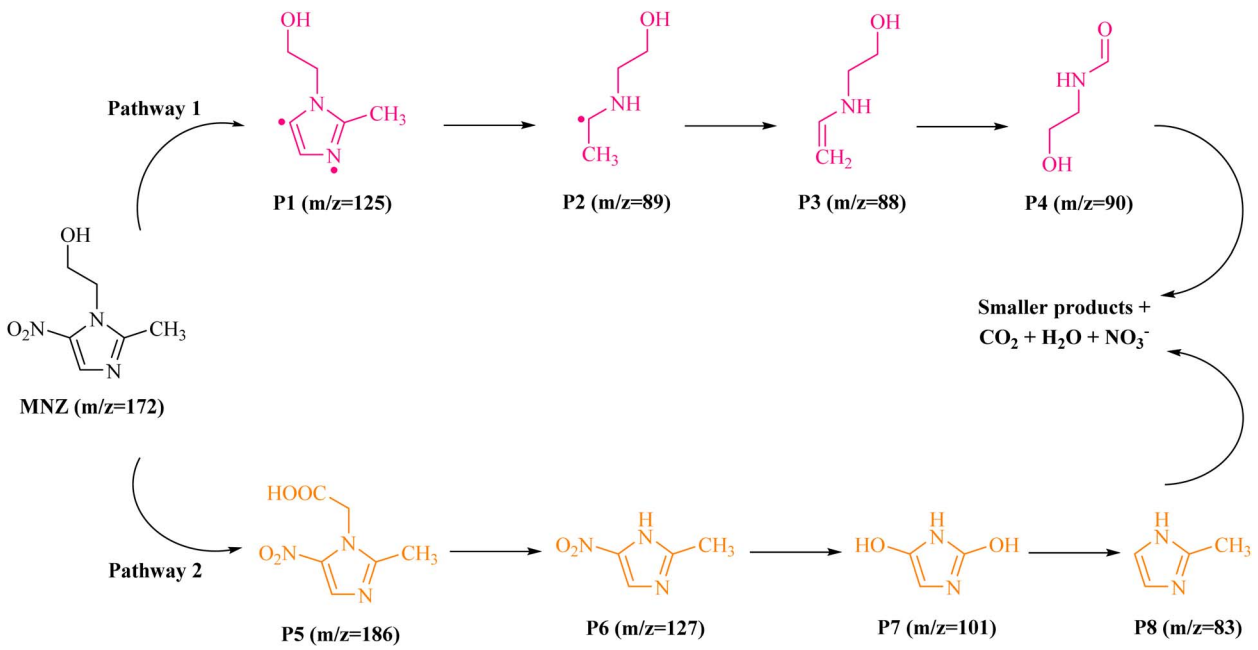

Fig. 10 Suggested MNZ degradation pathways using the Mn_3O_4/biochar/PMS system.

Open Access Article. Published on 02 June 2026. Downloaded on 6/17/2026 12:25:31 AM. This article is licensed under a Creative Commons Attribution-NonCommercial 3.0 Unported Licence.

$$SO_4^{\bullet -} + {-}OH \rightarrow SO_4^{2-} + {}^{\bullet}OH \quad (20)$$

$$2SO_5^{\bullet -} \rightarrow 2SO_4^{2-} + {}^1O_2 \quad (21)$$

$$2SO_5^{\bullet -} + H_2O \rightarrow 2HSO_4^{-} + 1.5{}^1O_2 \quad (22)$$

$$SO_4^{\bullet -}/{}^{\bullet}OH/{}^1O_2 + MNZ \rightarrow \text{Degradation products} \quad (23)$$

The intermediates of MNZ were examined using UPLC-Q-TOF-MS in order to get a better understanding of the degradation processes of MNZ in the Mn_3O_4/biochar/PMS system. During the degradation process, a total of eight degradation products were likely identified based on fragmentation structures. For the mitigation of MNZ using Mn_3O_4/biochar/PMS systems, there are two feasible degradation pathways based on fragmentation products (Fig. 10). The first pathway elaborates denitration and H-removal, that ultimately resulted in the production of a nitrogen–carbon-centered radical intermediate P1 (m/z = 125) due to the $SO_4^{\bullet -}$ radical assault on the MNZ imidazole ring. Subsequently, P1 underwent cleavage at the N=C junctions, yielding a product designated P2 (m/z = 89). The transformation of P2 produced an olefinic intermediate, P3 (m/z = 88), which was then oxidized to create P4 (m/z = 90).[71] Conversely, the second pathway commenced with the production of P5 (m/z = 186) and P6 (m/z = 127) *via* a hydroxyethyl cleavage reaction. Following this, P7 (m/z = 101) and P8 (m/z = 83) were produced through a series of nitro-reduction, N-denitration, and oxidation reactions.[72] Finally, the straightforward intermediates P4 and P8 underwent further degradation into smaller organic molecules, such as acetic acid, prior to complete mineralization.

3.6. Catalyst stability

Regarding catalyst reusability and stability, five uninterrupted trials were executed under controlled settings to measure the catalyst's potential for repetitive use in large-scale, economically feasible applications. After every trial, the Mn_3O_4/biochar was separated from the reaction mixture through centrifugation. Then, it was carefully rinsed and then dried at 70 °C overnight to prepare it for reprocessing in the succeeding cycle. The efficiency of MNZ exhibited a gradual decrease owing to the repeated operation of the catalyst. Fig. 11(a) illustrates that the

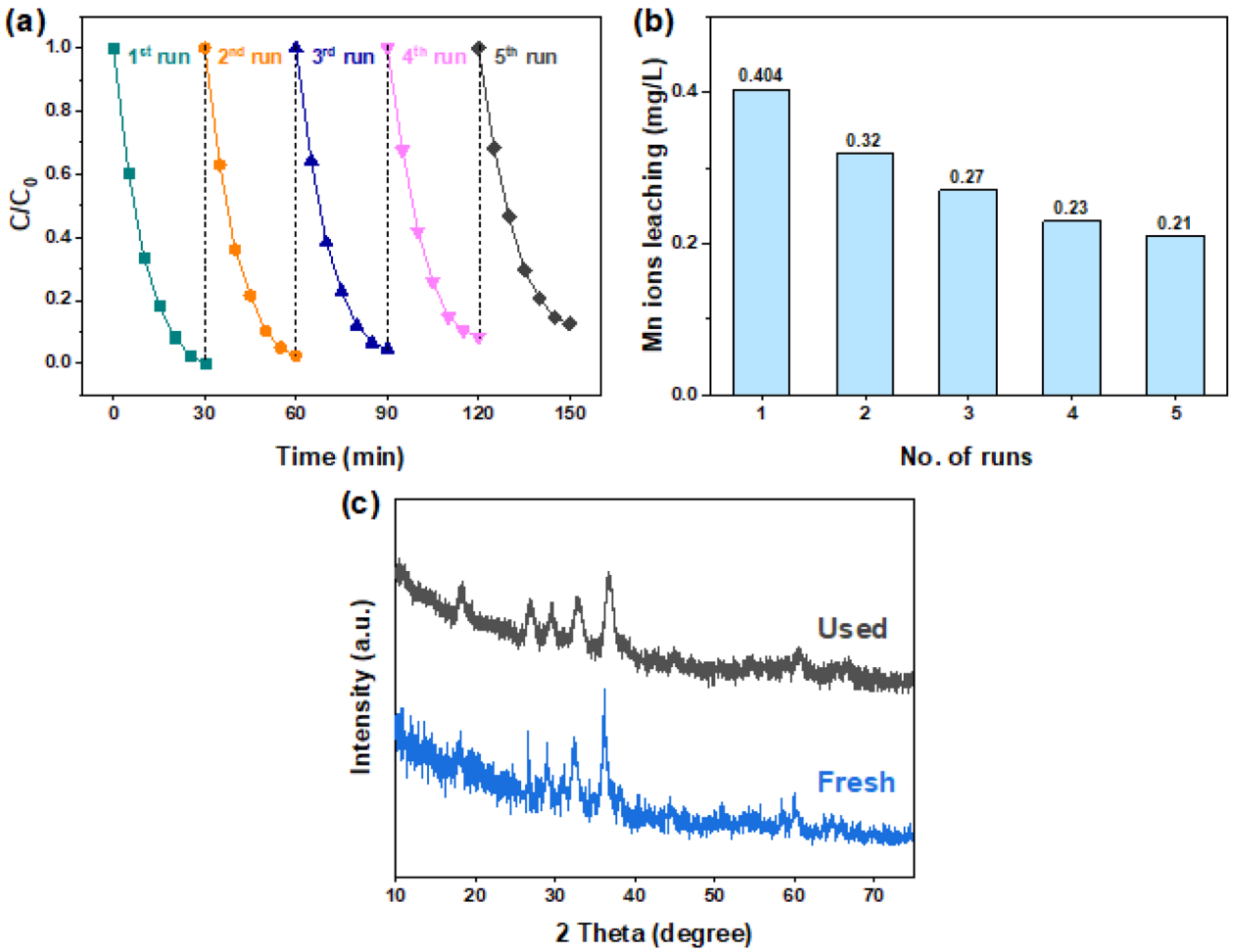

Fig. 11 (a) Reusability of Mn_3O_4/biochar/PMS system for the abatement of MNZ, (b) leaching amounts of Mn ions, and (c) XRD spectra of fresh and used (after five cycles) of Mn_3O_4/biochar catalyst.

© 2026 The Author(s). Published by the Royal Society of Chemistry

Open Access Article. Published on 02 June 2026. Downloaded on 6/17/2026 12:25:31 AM.
This article is licensed under a Creative Commons Attribution-NonCommercial 3.0 Unported Licence.

MNZ deterioration demonstrated a gradual reduction from complete degradation to 97.59%, 95.37%, 91.60%, and 87.45% during five consecutive cycles. The reduction in the degradation efficiency of Mn_3O_4/biochar involved several factors. First, partial leaching of active Mn species during reaction may decrease the number of accessible catalytic sites.[73] Second, the catalyst surface can be covered by the accumulation of chemical intermediates or by-products, which can obstruct the active sites and prevent the effective interaction between PMS and the catalyst. Third, the biochar support might undergo structural or surface changes, such pore blocking or surface oxidation, that might be responsible for the lower performance. Moreover, the repetitive use may lead to the agglomeration of Mn_3O_4 particles, which may further reduce the active surface area.

Fig. 11(b) depicts the quantified leaching of Mn ions, resulting in values of 0.404, 0.32, 0.27, 0.23, and 0.21 mg L^{-1} during five successive cycles. Furthermore, the XRD analysis of the used catalyst was performed to study the structural change after repeated use (Fig. 11(c)). The results suggest that the crystal structure of Mn_3O_4/biochar is mostly retained throughout reaction cycles. However, a small reduction in the peak intensity and small peak shifting was detected. These changes can be due to either partial structural distortion, surface modification or leaching of active Mn species to a small extent during the reaction phase. Finally, the aforementioned findings have validated the durability and reusability of Mn_3O_4/biochar catalyst, enabling its utilization in several degradation trials for MNZ abatement.

4. Conclusions

The present investigation established the efficacy of a Mn_3O_4/biochar catalyst, synthesized *via* a hydrothermal and co-precipitation method, in facilitating the activation of peroxymonosulfate (PMS) for the degradation of metronidazole (MNZ). Characterization of the catalysts revealed that Mn_3O_4/biochar possessed a more substantial surface area of 67.82 m^2 g^{-1}, whereas pure Mn_3O_4 presented a surface area of 45.29 m^2 g^{-1}. This disparity facilitated an increased availability of active sites for the triggering of PMS during the elimination of MNZ. Under ideal conditions, the MNZ attained complete degradation in 30 minutes having a k_{app} of 0.1402 min^{-1}. Conversely, the presence of inorganic ions, including Cl^-, NO_3^-, HCO_3^-, and HPO_4^{2-}, along with HA, substantially hindered MNZ decomposition. The trapping investigation confirmed that both radicals ($SO_4^{\bullet-}$/$^{\bullet}OH$) and non-radicals ($^1O_2$) were involved in the reduction of MNZ. The activation process provided additional confirmation of the redox cycling between Mn^{2+}/Mn^{3+}/Mn^{4+} during PMS activation, thereby elucidating its role in ROS generation and ultimate MNZ degradation. The Mn_3O_4/biochar catalyst exhibited stable and reliable catalytic performance along with low metal leaching across five cycles, thereby suggesting its suitability for repeated catalytic applications. Consequently, Mn_3O_4/biochar catalysts present a promising strategy for PMS activation in the degradation of antibiotics, thus offering an environmentally sound and dependable method for addressing environmental pollution.

Conflicts of interest

There are no conflicts to declare.

Data availability

Data will be available upon request.

Acknowledgements

The authors express their gratitude to the Princess Nourah bint Abdulrahman University Researchers Supporting Project (Grant No. PNURSP2026R12) and the Princess Nourah bint Abdulrahman University, Riyadh, Saudi Arabia. The authors extend their appreciation to the Deanship of Scientific Research, Islamic University of Madinah, Saudi Arabia, for funding this research work.

References

1 M. Rafiq, R. Ullah, A. Ahmed, X. Liu, M. Usman, Q. Cao, M. Adnan, M. Fayaz, W. Haider, B. Yu and H. Cong, Highly efficient degradation of norfloxacin by using Co_3O_4-CeO_2 as a heterogeneous catalyst through peroxymonosulfate activation: Characterization, catalytic performance and mechanism, *J. Water Proc. Eng.*, 2025, **71**, 107167.
2 Z. S. N. Ali, B. Janani, M. R. Shaik and S. S. Khan, Modulating electronic structures in ZrFe2O4/Zn3 (VO4) 2 by Ni and Mn co-doping for enhanced photocatalytic mineralization of ofloxacin, *J. Alloys Compd.*, 2025, 184480.
3 Y. Li, J. Bu, Y. Sun, Z. Huang, X. Zhu, S. Li, P. Chen, Y. Tang, G. He and S. Zhong, Efficient degradation of norfloxacin by synergistic activation of PMS with a three-dimensional electrocatalytic system based on Cu-MOF, *Separ. Purif. Technol.*, 2025, **356**, 129945.
4 A. G. Jerônimo, K. Amorim, W. Albuquerque, P. Trigueiro, Y. Romaguera-Barcelay, R. P. Feitosa, M. d. M. Orta, J. A. Osajima and R. R. Peña-Garcia, Rice husk ash–supported CdS composites for efficient photocatalytic degradation of metronidazole with minimized phytotoxicity, *J. Phys. Chem. Solids*, 2026, **213**, 113550.
5 C. Wang, H. Liu, G. Wang, W. Huang, Z. Wei, H. Fang and F. Shen, Visible light driven S-scheme heterojunction Zn3In2S6/Bi2MoO6 for efficient degradation of metronidazole, *J. Alloys Compd.*, 2022, **917**, 165507.
6 S. Chen, D. Wu, H. Xie, X. Sun and P. Xiao, Mechanistic and DFT studies on the degradation of metronidazole by cerium oxide-loaded iron-cobalt layered double hydroxide-activated calcium sulfite, *Separ. Purif. Technol.*, 2025, **357**, 130058.
7 D. Mei, S. Lu, L. Liang, S. Komarneni and J. Ma, Co_3O_4@CuO double core-shell hollow nanocages efficiently remove metronidazole by activating peroxymonosulfate under visible light, *Colloids Surf., A*, 2026, **729**, 138943.
8 S. He, R. Yin, T. Lai, Y. Zhao, W. Guo and M. Zhu, Structure–dependent degradation of nitroimidazoles by cobalt–manganese layered double hydroxide catalyzed peroxymonosulfate process, *Chemosphere*, 2021, **266**, 129006.

Open Access Article. Published on 02 June 2026. Downloaded on 6/17/2026 12:25:31 AM. This article is licensed under a Creative Commons Attribution-NonCommercial 3.0 Unported Licence.

9 S. He, R. Yin, Y. Chen, T. Lai, W. Guo, L. Zeng and M. Zhu, Consolidated 3D Co_3Mn-layered double hydroxide aerogel for photo-assisted peroxymonosulfate activation in metronidazole degradation, *Chem. Eng. J.*, 2021, **423**, 130172.
10 X. Chen, Z. Zhou, F. O. Gudda, L. Tang, H. Wang, B. Czech, P. Oleszczuk and Y. Gao, Hydroxyl groups and vacancy defects modified Mo_2C MXene as peroxymonosulfate activator for antibiotics degradation, *J. Clean. Prod.*, 2025, **486**, 144540.
11 X. Gao, D. Xing, D. Shu, G. Liu, C. Wang, Y. He, X. Cao and Y. Luo, Efficient solar-peroxymonosulfate activation via d-band modulation on $SrFeO_3/MoSe_2$ toward antibiotic contaminant removal, *J. Hazard Mater.*, 2025, **500**, 140367.
12 J. Y. Lu, Z. Q. Bu, Y. Q. Lei, D. Wang, B. He, J. Wang and W. T. Huang, Facile microwave-assisted synthesis of Sb2O3-CuO nanocomposites for catalytic degradation of p-nitrophenol, *J. Mol. Liq.*, 2024, **409**, 125503.
13 Q. Yong, L. He, F. Yao, S. Chen, Z. Wang, Z. Cao, W. Peng, X. Li, K. Luo and Q. Yang, Synergistic electro-activation of Peroxymonosulfate by F-FeP modified cathode for antibiotic degradation: Mechanism insight and practical implementation, *Separ. Purif. Technol.*, 2026, **394**, 137553.
14 H. Mao, Y. Hua, F. Chen, L. Zhuang, Z. Fan and C. Yao, The interfacial electric field enhanced piezo-catalytic performance of Bi2S3/Ni/CN composites for peroxymonosulfate activation advanced oxidation processes (AOP) systems, *J. Alloys Compd.*, 2024, **994**, 174645.
15 W. Xu, J. Liang, J. Li, S. C. Pillai, F. Liang, M. Li, K. Xiao, J. Li, Y. Wang, X. Jiang, Z. Liu, J. Beiyuan and H. Wang, Biochar encapsulated metal nanoflowers for high efficient degradation of metronidazole via peroxymonosulfate activation, *Separ. Purif. Technol.*, 2024, **328**, 125081.
16 Y. Wan, J. Liu, H. Wang, X. Song, W. Zhou, X. Liu, J. Zhang, Y. Yang, X. Zhang, B. Li and P. Huo, Photocatalytic peroxymonosulfate activation over S-scheme $Co_{1-x}S/g\text{-}C_3N_4$ heterostructure toward high-efficiency polyethylene terephthalate degradation, *Chem. Eng. J.*, 2025, **526**, 170725.
17 A. Ahmed, M. Usman, B. Yu, F. Gao, Y. Shen and H. Cong, Heterogeneous activation of peroxymonosulfate using superparamagnetic β-CD-$CoFe_2O_4$ catalyst for the removal of endocrine-disrupting bisphenol A: Performance and degradation mechanism, *Separ. Purif. Technol.*, 2021, **279**, 119752.
18 T. Zheng, P. Wang, B. Hu, C. Liu and R. Zhen, Deciphering Mn(II)/peroxymonosulfate system with nitrilotriacetic acid to degrade antibiotics: Roles of Mn species and interference of protein-like DOM, *Water Res.*, 2026, **297**, 125684.
19 Y. Ma, J. Wang, Z. Zhu, S. Pang and C. Sun, A dual-strategy for energy release from AP/Al via F-doped Cu2O Catalysis: Synergistic effects of surface oxygen vacancies and Cu+, *Ceram. Int.*, 2025, **51**, 44094–44106.
20 X. Ren, Z. Li, D. Huang, D. Yang, B. Zheng, J. Wang and N. Fu, Construction of a novel $Mn_3O_4/NiCo_2S_4$ composite catalyst for enhanced peroxymonosulfate activation toward rapid degradation of ofloxacin: Mechanistic and toxicity assessment, *Environ. Res.*, 2026, **294**, 123912.
21 Y. Zhang, P. Yu, X. Guo, L. Wang, W. Wang, L. Deng, H. Zhang, T. He, Z. Xiong and B. Lai, Iron single-atom catalysts drive peroxymonosulfate activation for efficient degradation of extracellular antibiotic resistance genes through singlet oxygen-mediated DNA damage, *Chem. Eng. J.*, 2025, **525**, 170041.
22 X. Wang, Z. Yao, F. Lv, Y. Geng, L. Chai, J. Wang and M. Ma, Spinel lattice distortion and oxygen vacancy dynamics in self-standing $NiCo_{2-x}Fe_xO_4$: mechanistic investigation of peroxymonosulfate activation pathways for antibiotic degradation, *Environ. Res.*, 2026, **289**, 123348.
23 X. Zhang, Q. Zhao, H. He, C. Zhang, L. Zhao and B. Li, Increasing Lewis acidic sites and promoting electron transfer of Mn_2O_3 by C-hybridization to improve the peroxymonosulfate activation for Bisphenol A degradation, *Environ. Res.*, 2025, **264**, 120409.
24 S. Zhuo, H. Ullah, X. Zhou, Z. Liu, S. Zhao, A. Xu, X. Li and A. Khan, Role of –OH groups on Mn_3O_4 heterogeneous catalyst surfaces in peroxymonosulfate activation: Degradation of levofloxacin via radical/nonradical pathways, *Appl. Surf. Sci.*, 2025, **685**, 162007.
25 F. Wang, M. Xiao, X. Ma, S. Wu, M. Ge and X. Yu, Insights into the transformations of Mn species for peroxymonosulfate activation by tuning the Mn_3O_4 shapes, *Chem. Eng. J.*, 2021, **404**, 127097.
26 J. Wu, H. Xie, G. Zhang, H. Lin, J. Xing, L. Wang and J. Xu, Oxygen vacancies engineering in Mn_3O_4 for regulating peroxymonosulfate activation and efficient bisphenol A degradation, *Chem. Eng. J.*, 2024, **499**, 156402.
27 Y. Li, X. Zhang, C. Huang and H. Lyu, A $g\text{-}C_3N_4/Mn_3O_4$/ZIF-8 composite for efficient degradation of dyes by activating peroxymonosulfate, *Opt. Mater.*, 2024, **149**, 114994.
28 H. Zhou, X. Zhu and B. Chen, Magnetic biochar supported α-MnO_2 nanorod for adsorption enhanced degradation of 4-chlorophenol via activation of peroxydisulfate, *Sci. Total Environ.*, 2020, **724**, 138278.
29 J. Fan, Q. Wang, W. Yan, J. Chen, X. Zhou and H. Xie, Mn_3O_4-$g\text{-}C_3N_4$ composite to activate peroxymonosulfate for organic pollutants degradation: Electron transfer and structure-dependence, *J. Hazard Mater.*, 2022, **434**, 128818.
30 M. Yang, Q. Huang, L. Xin, S. Zhang, J. Song and X. Li, Nitrogen-doped magnetic biochar derived from mulberry branch waste for efficient peroxymonosulfate activation and humic acid degradation via a dominant non-radical pathway, *Surf. Interfaces*, 2026, **83**, 108513.
31 B. Ma, J. Zhu, Y. Xu, L. Zhang, D. Liu, C. Chen and B. Sun, Photocatalytic degradation of methylene blue using ZnO modified with nano-biochar derived from bacterial cellulose, *Ceram. Int.*, 2025, **51**, 14948–14956.
32 J. Yuan, Y. Liu, Q. He, H. Wen, Z. Li, R. Lin, T. Chu, C. Peng, C. Zheng, H. Chen and Y. Tan, Phosphorus-modified biochar from salvia miltiorrhiza dregs: synthesis, characterization, and dual-functional synergy for heavy metal immobilization and soil fertility augmentation, *Biochar*, 2026, **8**, 30.
33 Z. Wang and G. Chen, Unlocking efficient redox cycling: The synergy of WC and Fe_3O_4 on biochar activated

© 2026 The Author(s). Published by the Royal Society of Chemistry

Open Access Article. Published on 02 June 2026. Downloaded on 6/17/2026 12:25:31 AM. This article is licensed under a Creative Commons Attribution-NonCommercial 3.0 Unported Licence.

peroxymonosulfate to degradate Orange G, *J. Water Proc. Eng.*, 2026, **85**, 109782.

34 T. Shen, A. Cheng, D. Chen, D. Wang, Y. Zhao and B. Zhang, Ginkgo leaf-derived Co_3O_4/N-doped biochar for enhanced rapid degradation of tetracycline in water via peroxymonosulfate activation, *J. Environ. Chem. Eng.*, 2026, **14**, 122053.

35 X. Lv, H. Cai, L. Yuan, S. Yang, X. Tu and J. Zou, Hierarchically porous N, S co-doped green bean biochar for efficient tetracycline degradation via peroxymonosulfate selective activation: Synergistic mechanism of adsorption and non-radical oxidation, *J. Water Proc. Eng.*, 2026, **83**, 109704.

36 X. Sun, K. Wu, G. Yang, F. Shen, S. Zhang, T. Wu, S. Sun, Y. Jiang and X. Wu, Synergistic effect of carbon defects and iron active sites in biochar-activated peroxymonosulfate for acetaminophen degradation: Unlocking the non-radical mechanisms, *Chem. Eng. J.*, 2025, **523**, 168775.

37 Z. Li, D. Liao, G. Tian, X. Fan, X. Chai, W. Chang, Y. Gao, B. Yuan, Z. Li, F. Wei and C. Zhang, Determination of Mn Valence States in Nanocatalysts During Sustainable Syngas Conversion, *J. Am. Chem. Soc.*, 2025, **147**, 32548–32559.

38 M. Challa, A. Narula and P. Deepthi, Nonlinear kinetics, isotherms, and thermodynamic approach in the carcinogenic ions elimination by Mn2. 7Al0. 3O4 sorbent, *Sci. Rep.*, 2025, **15**, 43296.

39 T. Kong, H. Wang, J. Sun, J. Liu, W. Zhang, W. Xing and R. Li, Mechanisms of nano magnetite-loaded biochar enhancing anaerobic digestion of food waste and effects of different loading methods and dosages on process performance and microbial characteristics, *Renew. Energy*, 2026, **267**, 125799.

40 D. Ding, S. Yang, X. Qian, L. Chen and T. Cai, Nitrogen-doping positively whilst sulfur-doping negatively affect the catalytic activity of biochar for the degradation of organic contaminant, *Appl. Catal. B Environ.*, 2020, **263**, 118348.

41 J. Chen, K. Chu, S. Sun, H. Chen, B. Song, J. Wang, Z. Liu and L. Zhu, Synthesis of magnetic core-shell Fe_3O_4-Mn_3O_4 composite for degradation of sulfadiazine via peroxymonosulfate activation: Characterization, mechanism and toxicity analysis, *J. Environ. Chem. Eng.*, 2023, **11**, 109230.

42 Y. Tang, Z. Wei, C. Wang, P. Ning, M. He, S. Bao, X. Sun and K. Li, One-step synthesis of magnetic catalysts containing Mn_3O_4-Fe_3O_4 from manganese slag for degradation of enrofloxacin by activation of peroxymonosulfate, *Chem. Eng. J.*, 2024, **499**, 156505.

43 Q. Gao, H. Ullah, Z. Ming, S. Zhao, A. Xu, X. Li and A. Khan, Synergistic degradation of p-nitrophenol using peroxymonosulfate activated with a bimetallic Mn_3O_4–Cu_2O catalyst: Investigation of strong interactions between metal oxides, *J. Environ. Chem. Eng.*, 2024, **12**, 113958.

44 A. Khan, K. Zhang, A. Taraqqi-A-Kamal, X. Wang, Y. Chen and Y. Zhang, Degradation of antibiotics in aqueous media using manganese nanocatalyst-activated peroxymonosulfate, *J. Colloid Interface Sci.*, 2021, **599**, 805–818.

45 Y. Wang, X. Wu, Q. Zhao, Y. Fu, X. Li, R. Su and M. Gao, Enhanced H_2O_2 production via S doped N-rich biochar natural air diffusion electrode in an electro-Fenton system for efficient tetracycline degradation, *J. Water Proc. Eng.*, 2026, **84**, 109749.

46 F. Jiang, Y. Zhang, X. Xu, Y. Mao, M. Wang, B. Yang, C. Zhang, X. Feng, H. Meng, F. Guo, Q. Han and S. Zhang, Application of cysteine with Cu2+ to strengthen Fenton-based treatment of coking wastewater used ferric sludge as a source of iron catalyst: Cl- removal and Fe3+/Fe2+ cycling, *J. Environ. Chem. Eng.*, 2025, **13**, 117556.

47 M. Aadil, M. E. A. Zaki, M. A. Rafea, A. M. Ahmed, S. Albarakati, M. R. El-Aassar, A. K. Alanazi and M. R. Alrahili, Design of $LaFeO_3$/$CuBi_2O_4$ composite for enhanced visible-light photocatalytic degradation of atrazine: Insights into activity, stability, and mechanism, *Inorg. Chem. Commun.*, 2026, **184**, 116022.

48 M. Ishfaq, M. Aadil, S. R. Ejaz, W. Hassan, N. M. Panduro-Tenazoa, M. E. El Sayed, M. N. Murshed and Z. M. El-Bahy, Synthesis of binary metal doped CeO2 via the subcritical hydrothermal method for photo-mineralizing methyl orange dye, *J. Alloys Compd.*, 2023, **960**, 170661.

49 Y. Wang, Y. Ren, X. Wang, Y. Yang, Z. Yang, D. Liu and T. Ni, Innovative Co3O4 nanosheet clusters: Harnessing abundant reactive sites for superior peroxymonosulfate activation and metronidazole degradation, *Surf. Interfaces*, 2025, **62**, 106322.

50 K. Xiao, F. Liang, J. Liang, W. Xu, Z. Liu, B. Chen, X. Jiang, X. Wu, J. Xu, J. Beiyuan and H. Wang, Magnetic bimetallic Fe, Ce-embedded N-enriched porous biochar for peroxymonosulfate activation in metronidazole degradation: Applications, mechanism insight and toxicity evaluation, *Chem. Eng. J.*, 2022, **433**, 134387.

51 X. Sun, H. Xi, Y. Dang and S. Yun, Layered double hydroxide-derived amorphous Ni–Fe phosphides for efficient activation of peroxymonosulfate to degrade metronidazole, *J. Environ. Chem. Eng.*, 2025, **13**, 116300.

52 H. Ren, C. Li, Z. Han, T. Li, X. Jin and R. Zhou, Magnetic mesoporous $FeCo_2O_4$–Fe_3O_4 microrods as novel peroxymonosulfate activators for effective metronidazole degradation, *J. Chem. Technol. Biotechnol.*, 2020, **95**, 3202–3212.

53 L. Hu, L. Shi, E. H. Dawolo, N. Ding and H. Liu, Cobalt-Modified Biochar from Rape Straw as Persulfate Activator for Degradation of Antibiotic Metronidazole, *Processes*, 2024, **12**, 1596.

54 M. Rafiq, A. Ahmed, M. Usman, R. Ullah, F. Gao, M. Mateen, B. Yu, Y. Shen and H. Cong, Efficient heterogeneous activation of peroxymonosulfate by manganese-doped $LaCoO_3$ perovskites for metronidazole degradation: A mechanistic study and reaction pathways, *J. Environ. Chem. Eng.*, 2023, **11**, 111608.

55 M. Yu, M. Chen, C. Yang, J. Niu, J. Zhang, S. Mu, R. Zhang, J. Ma and C. Liu, Sustainable Fe(II) oxidation/reduction and release/recovery dual cycle in a multi-chamber Fe(III)/Peroxymonosulfate electrochemical system: Application,

Open Access Article. Published on 02 June 2026. Downloaded on 6/17/2026 12:25:31 AM. This article is licensed under a Creative Commons Attribution-NonCommercial 3.0 Unported Licence.

mechanism, and optimization, *Chem. Eng. J.*, 2025, **512**, 162601.

56 M.-P. Zhu, J.-C. E. Yang, X. Duan, D.-D. Zhang, S. Wang, B. Yuan and M.-L. Fu, Interfacial $CoAl_2O_4$ from ZIF-67@γ-Al_2O_3 pellets toward catalytic activation of peroxymonosulfate for metronidazole removal, *Chem. Eng. J.*, 2020, **397**, 125339.

57 Y. Ma, C. Zhang, E. H. Dawolo, N. Ding and H. Liu, Fe/Mn-doped Chlorella biochar for enhanced metronidazole degradation via PMS activation: mechanistic insights into catalytic performance, *J. Mater. Chem. C*, 2025, **13**, 15532–15546.

58 Y. Guan, X. Tang, G. Zhou, H. Ding, S. Huang, Q. Chen, C. Zhao, T. Miao, L. Xu, Q. Han and L. Zhang, Oxygen vacancy-engineered Mn_3O_4 for efficient activation of peroxymonosulfate: Dominant non-radical pathway in antibiotic degradation in aqueous systems, *Separ. Purif. Technol.*, 2026, **388**, 136763.

59 Y. Zhang and W. Chu, g–C_3N_4 induced acceleration of Fe^{3+}/Fe^{2+} cycles for enhancing metronidazole degradation in Fe^{3+}/peroxymonosulfate process under visible light, *Chemosphere*, 2022, **293**, 133611.

60 J. Ding, A. Dou, T. Gu, G. Zhu, W. Tan, B. Wu and Q. Xu, Rapid degradation of sulfamethoxazole via peroxymonosulfate activation by hematite-loaded cobalt catalyst: Elucidating the role of singlet oxygen, *Surf. Interfaces*, 2025, **72**, 107398.

61 E. Sdoukou, M. Antonopoulou, C. E. Salmas, G. Z. Kyzas and I. Konstantinou, Peroxymonosulfate/persulfate activation by Ni (hydr)oxides loaded on tire char/activated char through radical and nonradical pathways for efficient degradation of emerging pollutants in waters and wastewaters, *J. Environ. Chem. Eng.*, 2025, **13**, 118834.

62 R. Ze, D. Liu, X. Liu, G. Huang, R. Wang, J. Zhou, X. Liu, X. Liu and H. Li, N-doped coal gangue as a superior peroxymonosulfate activator for rapid antibiotic degradation: mechanism and performance, *J. Water Proc. Eng.*, 2026, **85**, 109801.

63 A. Ahmed, M. Usman, Z. Ji, M. Rafiq, R. Ullah, B. Yu, Y. Shen and H. Cong, Reduced graphene oxide supported $CoFe_2O_4$ composites with enhanced peroxymonosulfate activation for the removal of sulfamethoxazole: Collaboration of radical and non-radical pathways, *J. Environ. Chem. Eng.*, 2023, **11**, 110452.

64 R. Yang, Q. Peng, A. Ahmed, F. Gao, B. Yu, Y. Shen and H. Cong, Yolk-shell Co_3O_4@Fe_3O_4/C nanocomposites as a heterogeneous fenton-like catalyst for organic dye removal, *Chem. Eur J.*, 2023, **29**, e202203097.

65 A. Ahmed, M. A. Rafea, S. Mubarik, M. E. A. Zaki, S. A. Al-Hussain, A. K. Alanazi, M. R. El-Aassar, M. Aadil and S. Saddeek, Advances in inorganic $NiFe_2O_4$/g-C_3N_4 composite catalysts: Synthesis, characterization, and application in peroxymonosulfate activation for antibiotic degradation, *Inorg. Chem. Commun.*, 2025, **182**, 115581.

66 Q. Sun, Y. Zhao, J. Zhang and J. Sheng, Efficient degradation of antibiotics over Co(II)-doped Bi_2MoO_6 nanohybrid via the synergy of peroxymonosulfate activation and photocatalytic reaction under visible irradiation, *Chemosphere*, 2022, **302**, 134807.

67 M. A. Alotaibi, A. I. Alharthi, A. Ahmed and A. Khalid, Highly efficient degradation of moxifloxacin through heterogeneous activation of peroxymonosulfate using Co_3O_4-g-C_3N_4 composites: Optimization of interfering factors, *Surf. Interfaces*, 2024, **52**, 104788.

68 W. Wu, L. Lu, D. Liao, B. Li, X. Liu, M. Muddassir, H. Sakiyama and J. Wang, Construction of a 2D polymer by rigid dicarboxylate and methylimidazol derivatives: structure and photocatalytic feature, *Inorg. Organomet. Polym. Mater.*, 2022, **32**, 875–882.

69 T. Yu, N. A. Al-Dhabi, W. Xing, Y. Zhu, S. Wang, K. Jiang and W. Tang, Highly efficient antibiotic decontamination and biotoxicity elimination with activity-stability considerations via encapsulated catalyst induced peroxymonosulfate activation, *J. Environ. Manag.*, 2025, **396**, 128078.

70 Y. Gao, W. Cao, K. Wang, H. Shi, S. Wang, Q. Meng, K. Du, C. Wang and J. Lin, Performance and mechanism of magnetic Fe3O4@ MnO2 catalyst for rapid degradation of methylene blue by activation of peroxymonosulfate, *J. Alloys Compd.*, 2024, **987**, 174144.

71 A. Ahmed, M. Usman, M. Rafiq, M. Adnan, R. Ullah, H. Cong and B. Yu, Enhanced activation of peroxymonosulfate by nanomagnetic $CoFe_2O_4$-CeO_2/g-C_3N_4 composites as a heterogeneous catalyst for metronidazole degradation, *J. Water Proc. Eng.*, 2024, **67**, 106266.

72 H. Ren, H. Liu, T. Cui, S. Liu, T. Ma, Z. Han and R. Zhou, Boosting the activation of Peroxymonosulfate and the degradation of metronidazole over $FeCo_2O_4$ quantum dots anchored on β-FeOOH Nanosheets: Inspired from octahedral Co(II) with missing angle, *Chem. Eng. J.*, 2022, **431**, 133803.

73 Q. Li, J. Liu, Z. Ren, Z. Wang, F. Mao, H. Wu, R. Zhou and Y. Bu, Catalytic degradation of antibiotic by Co nanoparticles encapsulated in nitrogen-doped nanocarbon derived from Co-MOF for promoted peroxymonosulfate activation, *Chem. Eng. J.*, 2022, **429**, 132269.

© 2026 The Author(s). Published by the Royal Society of Chemistry